

---

# UNIFIED INTERFACE FLUX EVALUATION IN A GENERAL DISCONTINUOUS GALERKIN SPECTRAL ELEMENT FRAMEWORK

---

**Boyang Xia**

Department of Engineering  
King's College London  
Strand, London, WC2R 2LS  
boyang.xia@kcl.ac.uk

**David Moxey**

Department of Engineering  
King's College London  
Strand, London, WC2R 2LS  
david.moxey@kcl.ac.uk

December 22, 2025

## ABSTRACT

High-order discontinuous Galerkin spectral element methods (DGSEM) have received growing attention and development in recent years, especially in the regime of computational fluid dynamics. The inherent flexibility of the DG approach in handling non-conforming interfaces, such as those encountered in moving geometries or *hp*-refinement, presents a significant advantage for real-world simulations. Despite the well-established mathematical framework of DG methods, practical implementation challenges persist to boost performance and capability. Most previous studies only focus on certain choices of element shape or basis type in a structured mesh, although they have demonstrated the capability of DGSEM in complex flow simulations. This work discusses low-cost and unified interface flux evaluation approaches for general spectral elements in unstructured meshes, alongside their implementations in the open-source spectral element framework, Nektar++. The initial motivation arises from the discretisation of Helmholtz equations by the symmetric interior penalty method, in which the system matrix can easily become non-symmetric if the flux is not properly evaluated on non-conforming interfaces. We focus on the polynomial non-conforming case in this work, but extending to the geometric non-conforming case is theoretically possible. Comparisons of different approaches, trade-offs, and performance of our initial matrix-free implementation are also included, contributing to the broader discourse on high-performance spectral element method implementations.

**Keywords** spectral/*hp* element method, discontinuous Galerkin methods, symmetric interior penalty method, matrix-free methods, SIMD vectorisation

## 1 Introduction

In computational fluid dynamics (CFD), high-order methods have gained popularity in research and industrial applications in recent years [1]. High-order methods, together with modern high-performance computing facilities, play an important role in achieving high-fidelity, multiscale resolved turbulent flow simulations in industrial applications. From a numerical perspective, diffusion and dispersion are greatly reduced at higher orders, meaning that such methods are ideally placed for tracking energetic flow structures such as jetting vortices [2, 3] or modelling problems involving high separation [4, 5] across long time- and length-scales. The use of a finite element discretisation also means that they retain the geometric accuracy required to model complex geometries and provide localised refinement, as needed for e.g. wall-resolved large-eddy simulations [6]. From a computing perspective, it is also well-documented that these high-order methods are well-suited to modern CPUs and GPUs due to higher operational intensity. For a desired level of solution error, we can reduce the total runtime by adjusting the polynomial order and mesh size accordingly. This has been highlighted in a range of popular frameworks, including deal.II [7], Dune [8], PyFR [9, 10] and MFEM [11], or efforts such as the CEED project [12].

Among the variety of high-order finite element methods, the discontinuous Galerkin (DG) method in particular is an area of rapid growth and development. DG is similar to classic finite volume methods (FVM), which allow discontinuity across element boundaries via a numerical flux and are broadly applicable across a range of hyperbolic problems. However, DG discretisations typically have a more compact stencil: that is, elements only need to communicate with their direct adjacent elements, rather than multiple layers of adjacencies, regardless of discretisation order [13]. In this manner, the treatment of complex non-conformal mesh interfaces in cases such as local  $hp$ -refinement and moving geometries is unified and independent of element order. Although the theoretical analysis of DG has been well studied in the past few decades [14, 15], their practical implementation in code varies according to different choices of the element type, basis, and target applications, requiring additional analysis and design. We are especially interested in these details, as they shape code design as well as attainable performance.

Although the theoretical analysis of DG has been well studied in the past few decades [14, 15], their practical implementation in code varies according to different choices of the element type, basis, and target applications, requiring additional analysis and design. We are especially interested in these details, as they shape code design as well as attainable performance.

The most popular element shapes in spectral element methods are quadrilateral and hexahedral elements, also known as tensorial elements since their expansions and quadratures are constructed via tensor product. Such elements possess several advantages. For instance, tensor computing techniques such as sum-factorisation [16] and collocation can be applied to reduce evaluation cost and enable matrix-free operators. There have been many encouraging developments towards practical, robust, and efficient fluid dynamics solvers based on hexahedral elements in recent years [17, 18, 19, 20, 21, 22], enabling larger-scale and more complex flow simulations.

The motivation of this work arises from the fact that the generation of high-quality, fully hexahedral meshes suitable for the simulation of realistic industrial geometries is an open and complex problem [23]. In these cases, the most common mesh decompositions involve either fully tetrahedral or mixed prismatic-tetrahedral meshes. For tetrahedra, prisms and pyramids, general tensorial expansions such as those presented in [24] and [25] are still possible. Although they result in higher computing cost relative to hexahedra, we can still benefit from matrix-free implementations and achieve over 50% of the peak performance of modern CPUs, by making good use of multi-level caches, vectorisation, and sum-factorisation in continuous Galerkin methods [26].

A secondary interest is non-conforming interfaces, which appear when adjacent elements are either misaligned (geometrical non-conforming) or have different orders (polynomial non-conforming). The most well-known approach to handle such cases is called the mortar element method [27], first considered for  $C^0$ -continuous spectral element methods [28, 29], but can also be applied to DG [30, 31, 32, 33].  $L^2$  projection between local elements and mortar elements is essential to retain convergence. In all previous publications, the projection is performed between the solution degrees of freedom, so that the inverse mass matrix is explicitly presented in the formulation, which is typically expensive to compute. Constructing mortar elements is cumbersome between unstructured triangular mesh interfaces; therefore, in these cases, we prefer point-to-point interpolation [31], which directly evaluates the adjacent solution at local points and computes the flux term locally. However, it is known to be sub-optimal in accuracy.

Our goal in this work is to address these gaps, by presenting a complete picture of formulation, implementation design and performance analysis for the SIPG discretisation of a Helmholtz operator on various element types. The paper is structured as follows. In section 2, we introduce the formulation of the method and its existing implementation within Nektar++. We then introduce an optimised workflow to evaluate any DG formulation, followed by general interface flux evaluation designs. Section 2.2 presents a theoretical analysis of the interior penalty method from a unique perspective, to illustrate how flux evaluation on non-conforming interfaces can affect the symmetry of systems. Based on the analysis, we propose two ways to handle non-conforming interfaces in section 3: one is to use sufficient quadrature, and the other is to define a shared trace space and unify the quadrature for both sides, similar to mortar elements. We discuss in detail how these two approaches can be implemented to achieve unified, low-cost flux evaluations for general spectral elements. In this work, we only focus on polynomial non-conforming cases, but extension to geometric non-conforming cases is also possible. Numerical validation is given in section 4. Different bases, quadratures, and shape types are tested to demonstrate that our implementation is unified for general spectral elements. Finally, a detailed performance benchmark of our initial matrix-free implementation is given to mark our current progress.

Table 1: Summary of elements and basis functions available in Nektar++ [25]

Shape type	Basis type	Tensor structure	B/I decomposition
Quadrilateral/ Hexahedron	Modal	standard	Yes
	Orthogonal	standard	No
	Lagrange-GLL	standard	Yes
	Lagrange-GL	standard	No
Triangle/ Tetrahedron	Modified modal	generalized	Yes
	Orthogonal	generalized	No
	Lagrange-Elec	No	Yes
Prism	Modified modal	generalized	Yes
	Orthogonal	generalized	No
	Lagrange-Elec	No	Yes
Pyramid	Modified modal	generalized	Yes
	Orthogonal	generalized	No

## 2 Basics and formulations

### 2.1 Spectral elements in Nektar++

The computing domain  $\Omega_h$  is discretized into non-overlapping elements  $\Omega_e$ :  $\Omega_h = \bigcup \Omega_e$  with boundary  $\partial\Omega_h$ . Similarly, element boundaries are denoted as  $\partial\Omega_e$ . This section gives an overview of how Nektar++ unifies different spectral elements. Details can be found in [24].

#### Bases and coefficient spaces

The basis (or shape) functions  $\phi(\boldsymbol{\xi})$  are defined on standard elements  $\Omega_{st}$  and the solution is approximated by expansions

$$u_h(\boldsymbol{\xi}, t) = \sum_i \phi_i(\boldsymbol{\xi}) \hat{u}_i, \quad (1)$$

where  $\hat{u}_i$  is the coefficient related with the  $i$ -th basis. solutions are stored as a vector of coefficients for all bases and elements,  $\hat{\mathbf{u}}$ , known as *coefficient* space.

The construction of a general tensorial basis for a general element of dimension  $d$  is documented in [24, 34], and involves a Duffy transformation [35] between the reference element  $\Omega_{st}$  with coordinates  $\boldsymbol{\xi}$ , and the so-called *collapsed coordinate* system  $\boldsymbol{\eta} \in [-1, 1]^d$ . Generally, this takes the form

$$\phi_i(\boldsymbol{\xi}) = \psi_{i_1}(\eta_1) \psi_{i_2}(\eta_2) \cdots \psi_{i_d}(\eta_d), \quad (2)$$

where  $\psi_{i_k}(\eta_k)$  is the basis function in coordinate direction  $k$ , and for hexahedra and quadrilaterals,  $\eta_k$  can be replaced by  $\xi_k$ . The basis functions available in Nektar++ are related to element shape types and summarised in Table 1. The modified  $C^0$  *modal basis* in [24] were designed for CG methods, as the basis functions possess a *boundary-interior decomposition*, making the system easier to assemble. In DG, this is not required but can be exploited to simplify the trace contributions to the element.

#### Quadrature and physical spaces

In general, arithmetic operations must be done in *physical* space within  $\mathbf{u}$ , a vector storing solution values at points  $\boldsymbol{\xi}_q$ . These points are also responsible for integration within the element, and one can increase the quadrature order to decrease aliasing error. In Nektar++, multidimensional quadrature is constructed by a tensor product of 1D quadrature

$$\int_{\Omega_e} u \, d\Omega \cong \sum_{p=1}^{N_{Q_1}} \sum_{q=1}^{N_{Q_2}} u(\xi_{1p}, \xi_{2q}) \omega_{1p} \omega_{2q} J(\xi_{1p}, \xi_{2q}) \quad (3)$$

as shown in Fig. 1, where  $N_{Q_i}$  are the number of quadrature points in dimension  $i$ ,  $\omega_{ij}$  are the corresponding quadrature weights, and  $J$  is the determinant of Jacobian matrix  $|\frac{\partial(x_1, x_2)}{\partial(\xi_1, \xi_2)}|$ . Gauss-Lobatto is typically used, which includes endpoints and allows boundary conditions to be easily imposed. However in non-tensorial elements, the Duffy transformation leads to a removable singularity at collapsed vertices. We can avoid special treatment of this point through the use of Gauss-Radau points, which exclude one endpoint, or Gauss-Legendre points, which exclude both endpoints.

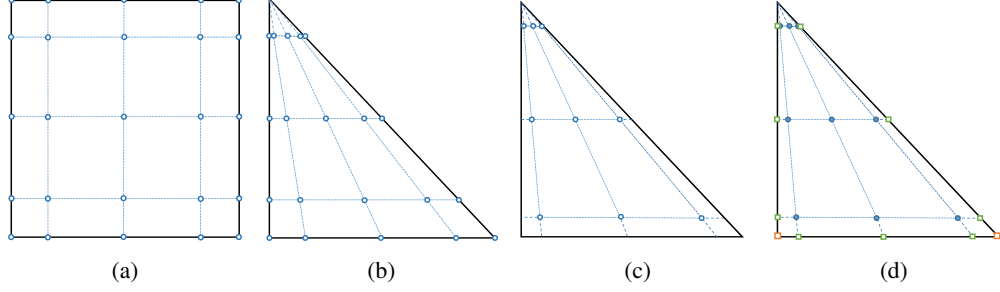


Figure 1: The distribution of Gauss quadrature points for quadrilateral and triangle elements. (a) Gauss-Lobatto-Legendre (GLL) points in a quadrilateral; (b) Gauss-Radau (GR) points on dimension 2 in a triangle; (c) Gauss-Legendre (GL) points in a triangle; (d) Gauss points with additional endpoints for quadrature on both elements and boundaries, which still maintains a standard tensor structure.

## 2.2 DG discretisation of the Helmholtz equation using SIPG

### Model problem and discretisation

Consider the Helmholtz problem given by  $-\nabla^2 u + \lambda u = -f$  defined on  $\Omega$  with  $\lambda \geq 0$ . The discretisation by the symmetric interior penalty Galerkin method (SIPG) on a single element reads [17]

$$(\nabla v_h, \nabla u_h)_{\Omega_e} + \lambda(v_h, u_h)_{\Omega_e} - (\nabla v_h, \frac{1}{2} \llbracket u_h \rrbracket)_{\partial\Omega_e} - (v_h, \{\!\{ \nabla u_h \}\!\} \cdot \mathbf{n})_{\partial\Omega_e} + (v_h, \tau \llbracket u_h \rrbracket \cdot \mathbf{n})_{\partial\Omega_e} = -(v_h, f)_{\Omega_e}, \quad (4)$$

where  $v_h$  is the test function for  $u_h$  space. The inner product is abbreviated by  $(v, u)_{\Omega} = \int_{\Omega} v \cdot u \, d\Omega$ . In the context of DG, information on the current and its adjacent element is usually denoted by superscripts  $+$  and  $-$ . The average operator  $\{\!\{ \cdot \}\!\}$  and jump operator  $\llbracket \cdot \rrbracket$  are defined as

$$\{\!\{ \mathbf{u} \}\!\} = \frac{\mathbf{u}^- + \mathbf{u}^+}{2}, \quad \llbracket \mathbf{u} \rrbracket = \mathbf{u}^- \otimes \mathbf{n}^- + \mathbf{u}^+ \otimes \mathbf{n}^+, \quad (5)$$

where  $\mathbf{n}$  is the outward unit normal vector, and  $\otimes$  denotes the tensor product. On the boundaries,  $\mathbf{u}^+$  and  $\nabla \mathbf{u}^+$  are determined by boundary conditions [17].

Eq. (4) is given from an element perspective. Summing over all elements restores the primal formulation [14]

$$(\nabla v_h, \nabla u_h)_{\Omega_h} + \lambda(v_h, u_h)_{\Omega_h} - (\{\!\{ \nabla v_h \}\!\}, \llbracket u_h \rrbracket)_{\Gamma} - (\llbracket v_h \rrbracket, \{\!\{ \nabla u_h \}\!\})_{\Gamma} + \tau(\llbracket u_h \rrbracket, \llbracket v_h \rrbracket)_{\Gamma} = -(v_h, f)_{\Omega_h}, \quad (6)$$

where  $\Gamma$  is the collection of all interior element interfaces and exterior boundaries: the *trace* space of the domain. To restore this bilinear form, two overlapping interior element boundaries will be considered as the same one; in other words, the inner product operator should be consistent for the elements on the two sides to achieve a symmetric system. One primary reason for choosing SIPG is that it can be solved by the conjugate gradient method, which is less complicated to compute than other Krylov methods such as GMRES. However, it is not guaranteed to converge if the system is not symmetric. This is in contrast to some other DG applications, where an inaccurate flux evaluation may not ruin the solution immediately. Our experience is that to achieve a truly symmetric SIPG formulation is not trivial for non-conforming discretisations: a detailed hands-on analysis is given in the appendix, showing how the flux evaluation affects symmetry. There are two basic strategies to resolve this issue: either to choose sufficient points to evaluate the quadrature accurately, or to unify  $\Gamma_l$  and  $\Gamma_r$  and let the inner product be evaluated by the same quadrature formula. The following section will discuss how we develop unified interface flux evaluations based on these two strategies.

## 3 Unified interface flux evaluation for general spectral elements

### 3.1 From basic operators to optimised solver workflow

It is necessary to first present an overview of how a matrix-free DG solver is implemented in Nektar++ before we discuss interface flux evaluation. The primary target is to evaluate the left-hand side (LHS) or right-hand side (RHS)

of a discretised equation. We prefer not to assemble the system matrix in advance but evaluate the results via a series of basic operators following its mathematical formula, which reduces memory access at runtime at the cost of increasing floating point operations, thus increasing the arithmetic intensity and the performance. To achieve this goal, the workflow must be carefully designed. Nektar++ provides a series of core elemental operators:

- **BwdTrans**: Evaluate the physical values  $\mathbf{u}$  from the coefficients  $\hat{\mathbf{u}}$  as in (1).
- **PhysDeriv**: Compute the derivative of  $\mathbf{u}$  using collocation differentiation [24]. Note that the physical points always have a tensorial structure, so PhysDeriv is the same for any element shape.
- **IProduct**: Perform an inner product within this element according to (3). If we extract the quadrature metric  $\omega$  and  $J$  out of the inner product, then this operation is essentially a transposed operation of BwdTrans.

Fig. 2a shows the basic workflow to evaluate the LHS or RHS of DG formulations; the actual implementation is shown in Fig. 2b and will be discussed in the following section. Starting from the solution unknowns  $\hat{\mathbf{u}}$ , we call BwdTrans to get physical  $\mathbf{u}$  then PhysDeriv to get derivatives. Physical  $\mathbf{u}$  and  $\nabla \mathbf{u}$  are used to evaluate the volumetric flux. Finally, we perform the inner product and add the contribution to LHS or RHS, in the coefficient space. This workflow is not unique: for example, one may consider combining BwdTrans and PhysDeriv to get derivatives directly from coefficient space. However, theoretical estimation [36] and our practice show this is more expensive than collocation differentiation PhysDeriv in cases without over-integration.

As for interface flux term evaluation, we need additional operators GatherInterp and ScatrInterp (or TracePhysEval and TraceIProduct). Broadly speaking, a general interface flux evaluation takes three steps:

1. Gather trace physical data from element physical data (GatherInterp), or evaluate them directly from element coefficients (TracePhysEval);
2. Compute the flux on the trace physical space, varying according to the problems;
3. Add trace physical data back to element trace physical space (ScatrInterp) and then perform inner product to get contributions to the LHS/RHS, or perform inner product on trace and transform the result back to element coefficient space directly (TraceIProduct).

The relative merits of these operators will be discussed in the following sections.

### 3.2 Obtaining trace data from elements

#### Direct evaluation of trace physical solution & derivatives

TracePhysEval in Fig. 2a is essentially a special version of BwdTrans and PhysDeriv. If  $\xi_p$  covers all quadrature points on the trace and  $\phi_i$  covers all bases of this element, then the resulting  $\phi_i(\xi_p)$  can be used to evaluate the physical solution on the trace. Sum-factorisation can also be applied to this operator:

$$u(1, \xi_{2q}, \xi_{3r}) = \sum_{i=1}^{N_P} \sum_{j=1}^{N_P} \sum_{k=1}^{N_P} \psi_i(1) \psi_j(\xi_{2q}) \psi_k(\xi_{3r}) \hat{u}_{ijk}, \quad 1 \leq q, r \leq N_{Q_\Gamma}, \quad (7)$$

which evaluates all solution values on the face  $\xi_1 = 1$ , with a nominal computing cost of  $N_P^3 + N_P^2 N_{Q_\Gamma} + N_P N_{Q_\Gamma}^2$ . TraceIProduct can be derived in the same way from (3). As for the derivative on the trace, we need  $\nabla \phi_j(\xi_p)$  that covers all the trace quadrature points and all the element bases, which is equivalent to  $\phi_i(\xi_q)$  times  $\nabla \ell_q(\xi_p)$ .

#### Gather & interpolate trace data from the element

GatherInterp is available when the quadrature points include the endpoints, such as the Gauss-Lobatto points. In this case the boundary quadrature points are a subset of element quadrature points, so we can directly gather trace data from the elemental physical space without any additional computing cost. If the trace points are different from local surface points, then additional Lagrange interpolation is required. For example, to interpolate from  $N_Q \times N_Q$  local face to  $N_{Q_\Gamma} \times N_{Q_\Gamma}$  trace space, the nominal computing cost of interpolation by sum-factorisation is  $N_Q^2 N_{Q_\Gamma} + N_Q N_{Q_\Gamma}^2$ . Recall that the trace space always has the same or higher quadrature order than its adjacent local element. The Lagrange interpolation will not deteriorate the polynomial order of the input, so we should obtain equivalent results as TracePhysEval.

To use Gauss points in GatherInterp as well, one possible way is to add auxiliary endpoints to cover boundary quadrature, as shown in Fig. 1d. The resulting physical space still has a standard tensorial structure, so the existing sum-factorisation operators can be directly applied.

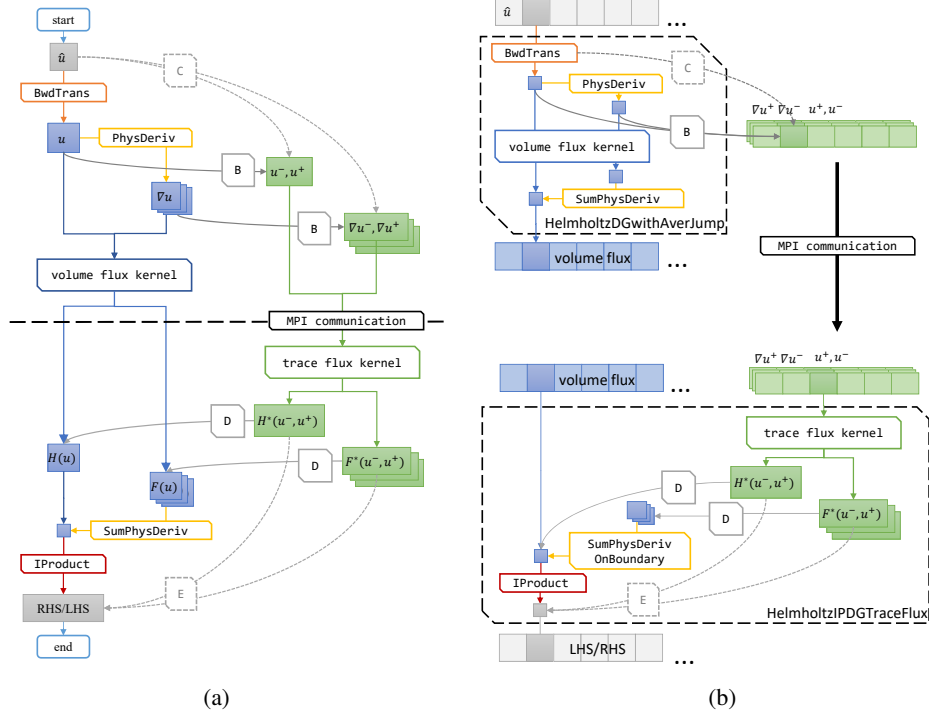


Figure 2: The optimised workflow to evaluate the LHS or RHS in a DG formulation. (a) The basic design; (b) The actual design with fused kernel and cache blocking

### 3.3 Handling non-conforming interfaces

#### Shared trace space

As discussed in section 2.2, one strategy for a consistent flux evaluation on non-conforming interfaces is to unify the trace quadrature for two adjacent elements. So we begin by introducing the *trace space* to Nektar++, a non-overlapping interface shared by two adjacent elements, as shown in Fig. 3. In Nektar++, this concept is achieved by creating a list of trace *Expansion* objects, on which we can build required operators. As a general rule, the quadrature order on the trace should be at least the same as the higher-order side to achieve better accuracy.

*TraceIPProduct* performs the inner product on the shared trace and projects results back to the local element coefficient space. Since the shared trace space is inconsistent with the local element on one side, we need to create a special set of *Expansion*, which may differ from the local elements, to get the corresponding  $\phi_i(\xi_q)$ , and other geometric information used in operator *TraceIPProduct* and *TracePhysEval*. They are called *trace-conforming element* because the geometry and bases are the same as the local element, while the physical points are consistent with the trace. These *Expansions* serve as a bridge between the shared trace and the local element.

The shared trace space is conceptually the same as the *mortar elements*, which are traditionally used to bridge between non-conforming interfaces in continuous spectral element meshes. In the mortar element method, we first project solutions from the local elements on the two sides to the mortar element. Then we evaluate the flux in the mortar space and finally project the flux back to the element of each side. For CG or DG methods, an  $L^2$  projection is a natural choice [30] and is given by

$$\hat{u}^\Xi = (\mathbf{M}^\Xi)^{-1} \mathbf{S}^{\Omega_e \rightarrow \Xi} \hat{u} \quad (8)$$

where the superscript  $\Xi$  denotes the objects of the mortar element,  $\mathbf{M}^\Xi$  is the standard elemental mass matrix of mortar element  $M_{ij}^\Xi = (\phi_i^\Xi, \phi_j^\Xi)_\Xi$ , and  $\mathbf{S}^{\Omega_e \rightarrow \Xi}$  is the transfer mass matrix from local element to mortar element  $S_{ij}^{\Omega_e \rightarrow \Xi} = (\phi_i^\Xi, \phi_j)_\Xi$ . Previous studies considered nodal elements with collocation, so that the mass matrix is diagonal and easy to apply. However, in a general spectral element framework, the mass matrix is dense and generally differs per element, making computing and multiplying the inverse mass matrix in every projection an expensive part of the method. Additionally, as mentioned in section 2.1, the flux calculation needs to be performed in physical space rather

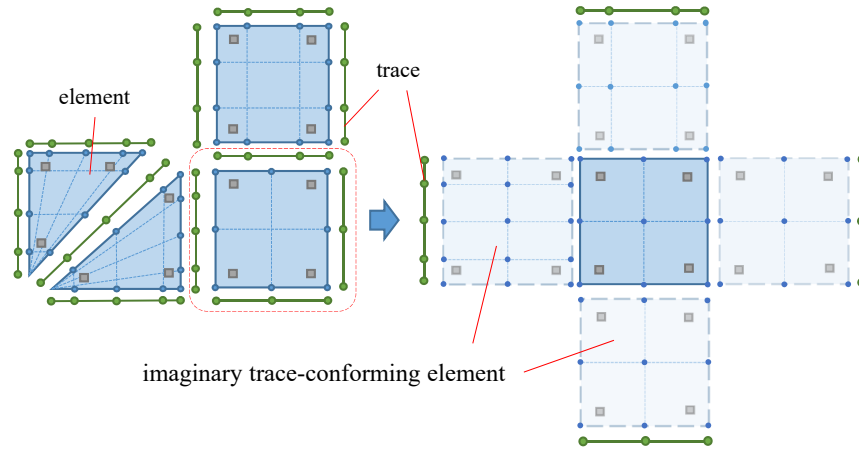
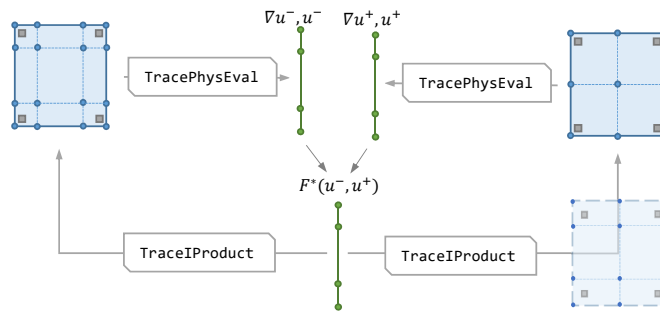
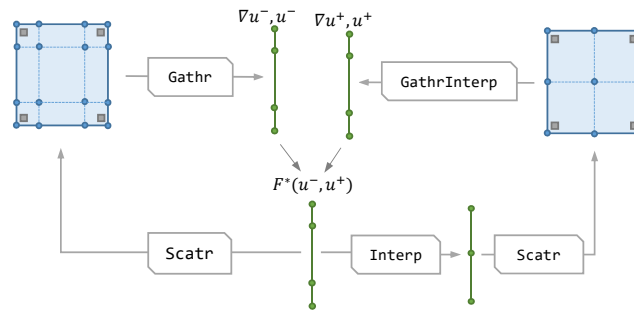


Figure 3: The concept of the shared trace space and trace-conforming element, which has the same bases and geometry as the local element, but the quadrature points are the same as the linked trace.



(a)



(b)

Figure 4: Two different approaches handle non-conforming interfaces. (a) Flux evaluation via shared trace; (b) Flux evaluation by point-to-point interpolation.

than coefficient space, which leads to an additional call to `BwdTrans`. Typically, we only need to perform the inner product at the final step and multiply by the inverse mass matrix if required. The projection between the coefficient space is sub-optimal and should be avoided if possible. To achieve this, Eq.( 8) can be rewritten as

$$\int_{\Xi} \phi_i^{\Xi}(\mathbf{z}) u^{\Xi}(\mathbf{z}) d\Xi = \int_{\Xi} \phi_i^{\Xi}(\mathbf{z}) u(\boldsymbol{\xi}) d\Xi \quad (9)$$

In the case that the mortar element is aligned with the local element, the local coordinate  $\mathbf{z}$  and  $\boldsymbol{\xi}$  are the same. If our goal is to retrieve the physical solution on the mortar elements that satisfy the above  $L^2$  relation, we can imprint the mortar quadrature points  $\mathbf{z}_q$  to the local element and evaluate the solution on those points:

$$u^{\Xi}(\mathbf{z}_q) = u(\mathbf{z}_q) = \sum_j \phi_j(\mathbf{z}_q) \hat{u}_j. \quad (10)$$

This is the approach we adopt in our current design, so that the flux evaluation via shared trace space in the present work is mathematically equivalent to the mortar element method, but simplified in computation. It can also be extended to handle geometric non-conforming interfaces as the mortar element does, although this is beyond the scope of the current work.

### Point-to-point interpolation

In `ScatrInterp`, we first use Lagrange interpolation to transform data from the adjacent trace space into the local trace space, and then scatter the trace data back to the local element, with inner products evaluated in the local element space separately, as shown in Fig. 4b. The drawback is that we cannot achieve symmetrical systems in all cases, due to the interpolation from higher order to lower order. Following the analysis in the appendix, the matrix  $\mathbf{M}_C$  and  $\mathbf{M}'_C$  in the case of point-to-point interpolation becomes

$$\begin{aligned} M_{C(j,i)}^T &= \sum_{p=0}^{N_{Q_l}} \phi_j^l(\xi_p) (\omega_p J_p) \mathbf{n}_p^l \cdot \sum_{q=0}^{N_{Q_r}} \ell_q(\xi_p) \nabla \phi_i^r(\xi_q) \\ M'_{C(i,j)} &= \sum_{q=0}^{N_{Q_r}} \nabla \phi_i^r(\xi_q) \cdot (-\mathbf{n}_q^l) (\omega_q J_q) \sum_{p=0}^{N_{Q_l}} \ell_p(\xi_q) \phi_j^l(\xi_p) \end{aligned}$$

To ensure  $\mathbf{M}_C^T = -\mathbf{M}'_C$ , we need to satisfy two conditions:

1.  $N_{P_l} < N_{P_r} \leq N_{Q_l} < N_{Q_r}$  or  $N_{P_l} > N_{P_r} \geq N_{Q_l} > N_{Q_r}$ . This is obvious because the polynomial degree should not decrease after interpolation from the higher-order to the lower-order side.
2. The quadrature on the lower-order local trace should still be accurate for the integrand. The integrand can be up to  $(N_{P_r} - 1) + (N_{P_l} - 1) + 3p_{\text{geom}}$ , where  $p_{\text{geom}}$  is the polynomial degree of geometric mappings, and the multiple 3 includes  $J$ ,  $\mathbf{n}$  and  $\frac{\partial \mathbf{x}}{\partial \boldsymbol{\xi}}$ . The quadrature degree of exactness should be no less than that.

These conditions can be difficult to fulfill with arbitrary element shapes and orders. However, the reason we still consider this method is that it is simple to implement and can be easily applied to arbitrary non-conforming interfaces, particularly in 3D where mortar elements of unstructured triangles are very hard to construct. Moreover, this approach is also easier to achieve higher performance, as shown in section 5. A practical tip we can suggest to help alleviate the symmetry error is to insert a *transition layer*, as seen in Fig. 5, at a price of greater computing cost, which is generally sufficient to resolve conjugate gradient convergence issues in the current application. For example, a  $P4Q5$  (4 coefficients, 5 GLL points) element cannot be the neighbour to the  $P2Q3$  elements. After adding such a transition layer, which has the same coefficients as the lower-order elements but the same quadrature points as the higher-order element, the direct neighbours now become  $P2Q5$ - $P4Q5$  and  $P2Q5$ - $P2Q3$ . The former has a conformal trace space. As for the latter, we only need to ensure the  $P2Q3$  has sufficient quadrature accuracy for its local trace evaluation to achieve a symmetric system. This makes sense in adaptive  $p$ -refinement since the background mesh  $P2Q3$  will not be affected by the local refinement.

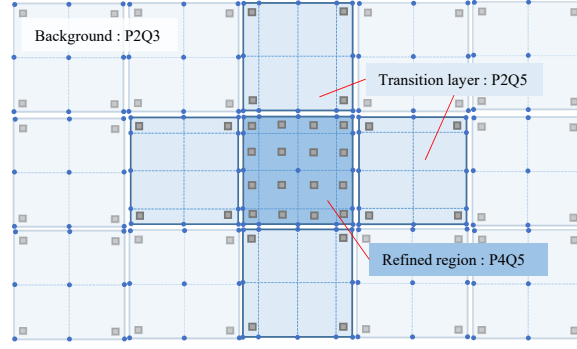


Figure 5: The transition layer around a  $p$ -refined region. The elements in the transition layer have the same points as the  $p$ -refined region, but the same coefficients as the background region.

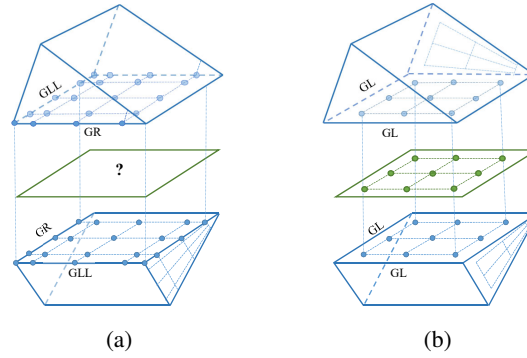


Figure 6: If collapsed coordinates are not aligned to the adjacent element, we cannot construct trace points that conform to Gauss-Radau points on both sides as shown in (a), but this is possible with rotationally-symmetric Gauss points, as shown in (b).

### 3.4 Other implementation issues

#### Singular vertices in collapsed coordinates

As mentioned previously, we avoid evaluating the derivative on singular vertices in collapsed coordinates of a simplex using either Gauss or Gauss-Radau points. Generally speaking, when constructing the trace-conforming elements, if the point distribution on a face or an edge is not rotational symmetric, then the local points on the two sides of the shared trace may be misaligned. Nektar++ can adjust the vertex of tetrahedra to ensure the top singular vertex of adjacent elements is always aligned. However, this cannot cover all the cases. Fig. 6a reveals an exception that that we cannot construct trace quadrature points that conform to both sides if Gauss-Radau points are used on a quadrilateral face due to non-symmetrical point distribution. The best and cheapest solution is using Gauss points, which are rotationally symmetric, as shown in Fig. 6b.

#### Exploiting boundary/interior decomposition

Boundary/interior decomposition is not required for DG. But with this property, the solution on the boundary only depends on certain coefficients that correspond to that boundary surface, known as the boundary modes [25]. This immediately provides an opportunity to reduce BwdTrans computing cost in the TracePhysEval. We can use a smaller basis matrix  $\phi_i(\xi_q)$  where  $\phi_i$  only includes boundary bases. The matrix size is reduced to  $N_P^{d-1} \times N_{Q_r}^{d-1}$  and the sum-factorisation cost is  $N_P N_{Q_r}^2 + N_P^2 N_{Q_r}$  in a hexahedron. Such boundary/interior decomposition is only valid for solution variables, but not for derivatives. So the overall cost reduction is modest.

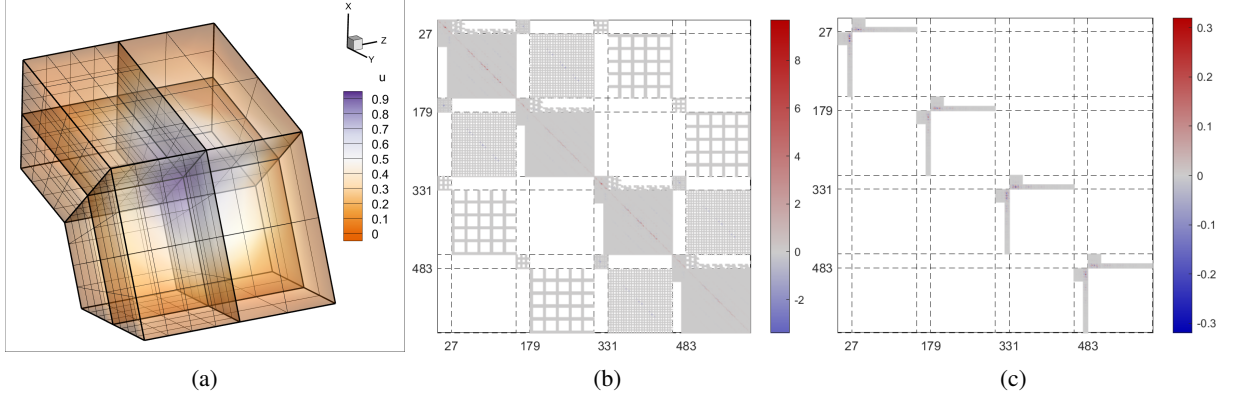


Figure 7: A critical case for point-to-point interpolation:  $P3Q4$  mixed with  $P5Q6$ . (a) The computing domain; (b) Sparsity pattern of the system matrix  $\mathbf{A}$ ; (c) Sparsity pattern of  $\mathbf{A} - \mathbf{A}^T$

Table 2: The analysis results of mixed-order cases shown in Fig. 7, by point-to-point interpolation. All cases use GLL points and Lagrange bases.

coefficient and quadrature	$P3Q4$ - $P5Q6$	$P3Q5$ - $P5Q6$	$P4Q5$ - $P5Q6$
$N_{P_r} \leq N_{Q_l}$ ?	No	Yes	Yes
required quadrature degree	$2 + 4 + 1 = 7$	$2 + 4 + 1 = 7$	$3 + 4 + 1 = 8$
actual quadrature degree	$4 \times 2 - 3 = 5$	$5 \times 2 - 3 = 7$	$5 \times 2 - 3 = 7$
$\frac{\ \mathbf{A} - \mathbf{A}^T\ _1}{\ \mathbf{A}\ _1}$	0.0252	$2.5 \times 10^{-18}$	0.0013
CG iterations to $10^{-9}$	-	62	69
GMRES iterations to $10^{-9}$	61	62	63
$L_2$ error	$1.52 \times 10^{-2}$	$1.08 \times 10^{-2}$	$8.96 \times 10^{-4}$

## 4 Numerical validation

In this section, we provide a numerical validation of the concepts introduced in the previous section by examining convergence order for the Helmholtz equation. To achieve this, we consider the sinusoidal solution

$$u(x, y, z) = \sin(kx) \sin(ky) \sin(kz). \quad (11)$$

with a corresponding manufactured forcing term  $f$  given as

$$f = -(\lambda + 3k^2) \sin(kx) \sin(ky) \sin(kz). \quad (12)$$

### 4.1 Validation and comparison with point-to-point interpolation

We start with basic validation by checking if the system matrix is symmetric in the cases of local  $p$ -refinement with  $k = \pi/2$ . The domain is a sector filled with  $2^3$  linear-shape hexahedra, where the elements use a Lagrange basis and independent GLL quadrature points. Boundary conditions are set to Dirichlet conditions consistent with the manufactured solution. To test the non-conforming implementation, half of the domain has a different polynomial order. For point-to-point interpolation, the case  $P3Q4$ - $P5Q6$  is critical, which leads to a non-symmetric system, as shown in Fig. 7. The non-symmetric entries all come from the off-diagonal part, such as the matrices  $M_C$ ,  $M_D$  and  $M_G$  in the appendix. Although the difference in  $\|\mathbf{A} - \mathbf{A}^T\|_1$  is less than 3% of  $\|\mathbf{A}\|_1$ , it is enough to prevent convergence, although solution via GMRES at equivalent accuracy is possible, as shown in Table 2. The table also shows that the system is exactly symmetric with  $P3Q5$ , which follows our previous analysis.

### 4.2 $p$ -refinement convergence rate

We now consider a convergence study of the SIPG Helmholtz solver with local polynomial refinement, for which we select a larger wavenumber  $k = 2\pi$ , so as to require higher resolution to attain accurate results. The cube domain is filled with  $N_x^3$  structured hexahedra. We subdivide each hexahedron into either 6 tetrahedra or 2 prisms to create

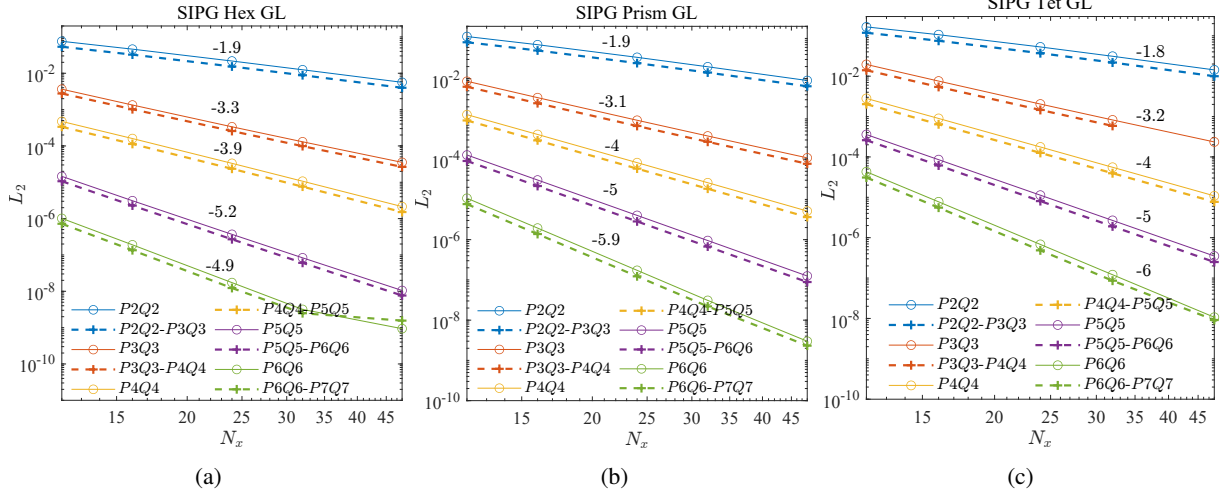


Figure 8: The convergence rate of a sinusoidal problem with local  $p$ -refinement. (a) Hexahedral mesh; (b) Prismatic mesh (c) tetrahedral mesh. The numbers are the slopes of the curves.

meshes with different element shapes but similar resolutions. All elements use the orthogonal basis, GL points and  $N_Q = N_P$ . Half of the domain is refined by adding 1 to the element order.

Fig. 8 presents the relation between  $L^2$  error and mesh resolution  $N_x$  with different polynomial orders and element shapes. From the slopes given in the figure, the SIPG Helmholtz solver achieves around  $N_P$  order convergence rate as expected. The locally refined cases also show a similar convergence rate with respect to the non-refined cases, and the error is only slightly lower, which is expected since only half the domain is refined. Typically the error contributed by higher-order discretisation is significantly smaller than the lower-order one, so the total error is dominated by the lower-order region.

To better show the effectiveness of local  $p$ -refinement, we manufacture a problem with a Gaussian pulse solution

$$u(x, y, z) = \exp\left(\frac{x^2 + y^2 + z^2}{a^2}\right) \quad (13)$$

within the same cube domain  $[-1, 1]^3$ . We select a character radius  $a = 0.2$  and the refined region is a cube in the middle of the domain  $[-0.5, 0.5]^3$ , enough to contain the pulse. Outside the refined region, the solution is nearly zero, so the error mostly depends on the refined region. This is confirmed in Fig. 9, where the locally refined case now achieves error magnitudes and convergence rates similar to the uniform high-order case, but with a lower number of degrees of freedom.

## 5 Matrix-free implementation and performance benchmark

In this section, we examine the high-performance implementation of the formulation of the previous sections, and outline the results from benchmarking that show the effective performance of the method on unstructured meshes.

### 5.1 Design choices in Nektar++

Efficient matrix-free kernels for core elemental operations are the foundation to achieve high performance, and Nektar++ already has these operators for various shape types [26]. The design choices we made in Nektar++ for any matrix-free implementations are:

- Disassemble a complex operator to lower-level operators like BwdTrans, where sum-factorisation or collocation can be applied, and basis or geometric data can be shared across elements or operators.
- Evaluate all other complex coefficients based on the pre-computed shared geometric information, Jacobian  $J$  and derived factor  $\frac{\partial x}{\partial \xi}$ . This is a trade-off between data size and computing cost.
- Provide specialized kernels for *regular* and *deformed* elements, since geometric information is constant for regular shape but spatially varying in deformed (curvilinear) elements. In the former case, we only need to

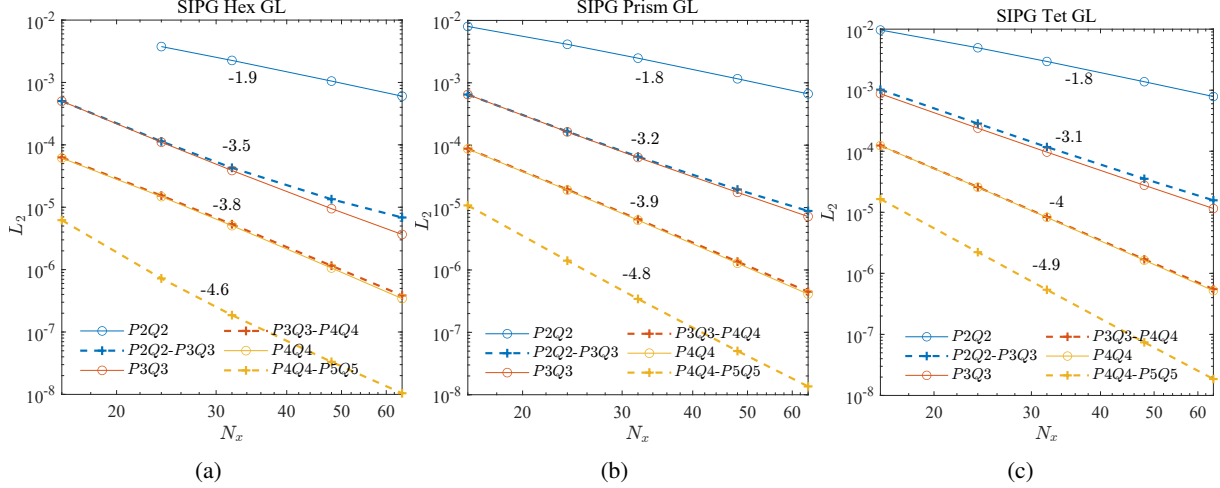


Figure 9: The convergence rate of the Gaussian pulse problem with local  $p$ -refinement. (a) Hexahedral mesh; (b) Prismatic mesh; (c) tetrahedral mesh. The numbers are the slopes of the curves.

load one Jacobian value or one face normal, and apply it to all points, which significantly reduces the memory load demands and increases arithmetic intensity.

- Elements of the same shape, basis and order are grouped and processed together, so that we can reuse the basis data when processing each element. To reuse geometric data as well and avoid writing large intermediate results to main memory, we try to perform as many operations as possible on a small group of elements before we write final results to memory and move to the next. This is illustrated in Fig. 2b and called cache blocking or kernel fusing in some literature. Kernel functions are force-inlined to reduce overheads.
- Interleave data layout across elements for more efficient SIMD vectorisation. For example, the data with the same local index from 4 elements are stored contiguously in memory. These data will be directly loaded into vector registers and processed by SIMD (single instruction, multiple data) instructions such as AVX2 or AVX512 (Advanced Vector eXtensions). In other words, each operator in Nektar++ can process 4 to 8 elements at a time.
- Generate separate kernels for different orders so that the loop bounds and local temporary memory sizes are all compile-time constants. In these cases, compilers can more aggressively optimise through loop unrolling and fusion.

As for parallel execution, Nektar++ only exchanges trace data with adjacent mesh partitions, instead of setting up *ghost* elements around the partition and exchanging the data of a whole element. This reduces the data size in communications, especially for high orders. Synchronisation is required during communication to avoid data racing. (We note it is also possible to overlap communication and computation to hide the communication costs, although we do not do this presently.) Our full workflow (LhsEval) is split into three sequential parts as shown in Fig. 2b:

1. `HelmholtzDGwithAverJump`: Evaluates Helmholtz volume flux and gets the average or the jump data on the traces.
2. `MPIexchange`: Sends trace data to adjacent partitions and also receives data from them.
3. `HelmholtzIPDGTraceFlux`: Evaluates all the interface fluxes and add their contribution back to the element space.

Both `HelmholtzDGwithAverJump` and `HelmholtzIPDGTraceFlux` are optimised fused kernels that process only a small group of elements at a time. We minimise the access to the global memory to only inputs and outputs at the beginning or the end of the fused kernel. The sub-operators only write intermediate results to a small temporary memory, which should stay in the cache and be accessed efficiently by the current or the next sub-operator. In this particular SIPG Helmholtz solver, we only need  $\{\{\nabla u\}\} \cdot \mathbf{n}$  and  $\llbracket u \rrbracket \cdot \mathbf{n}$  to evaluate all the flux shown in Eq. (4). So instead of exchanging four primitive variables (one  $u$  and three  $\nabla u$ ), we only exchange two variables to save communication costs.

We have two options to obtain trace data (`GathrInterp`, `TracePhysEval`) and two options to handle non-conforming interfaces (`ScatrInterp`, `TraceIProduct`). As for implementation, the concerns focus on ease of integration into

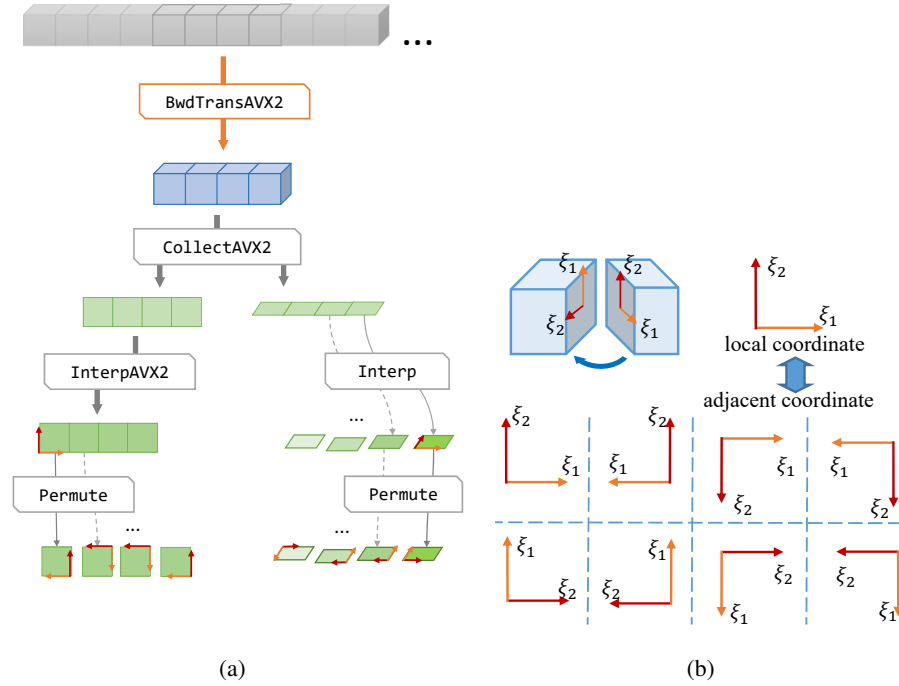


Figure 10: (a) The vectorisation strategy for gathering and interpolating trace data, and (b) the orientations between adjacent faces.

the framework and the potential to achieve higher performance. The first observation is that when interfaces are conforming, `GathrInterp` and `ScatrInterp` only involve memory transfer and have no floating-point cost. After `ScatrInterp`, only 1 `IProduct` on the whole element is performed. In contrast, we have to do `TraceIProduct` for every edge or face of the element, which is more expensive, as confirmed in both previous studies [31] and the present study. We therefore choose `GathrInterp` and `ScatrInterp` as the primary design, with `TraceIProduct` only enabled on non-conforming interfaces if required.

Our matrix-free implementation of `GathrInterp` and `ScatrInterp` follows the design choices above. In an arbitrary unstructured mesh, two adjacent elements may have different trace spaces and also different orientations, as shown in Fig. 10b. In three-dimensional space, there can be at most 8 different orientations, but usually, only a few orientations may appear in a practical mesh, and can be further reduced by deliberately swapping element local coordinates during the pre-processing stage. So the detailed process of operator B actually takes three steps:

1. **Gather:** Gather local trace physical data from the element's physical space.
2. **Interpolation:** If local and adjacent trace spaces differ, perform interpolation.
3. **Permutation:** If the local trace has different orientations, permute the trace data so that the storage order is the same as the adjacent space.

If the  $i$ -th trace of all elements in this group has the same interpolation configuration, we can perform gathering and interpolation in batch mode, using explicit SIMD instructions. Otherwise, only task 1 can be processed in batch mode and the other two must be done on a single trace at a time. This is illustrated in the Fig. 10a. The runtime efficiency, therefore, depends on how many elements of the same type and how many traces of the same type can be grouped together, which should be done during the preprocessing of the mesh.

Note that we do not claim the above design choices are the best overall: indeed, several were made to maintain compatibility with the existing codebase. The efficient implementation of DG operators, especially the face integral, is formally studied by Kronbichler et al. [37] in the deal.II framework and many design choices are tested and compared. Recently this was also studied in the Dune framework [19] with some different design choices, and excellent performance results were reported [38]. It is necessary to highlight the major differences between our designs.

Table 3: Hardware specifications and software configurations used for performance benchmarks

CPU Model	Xeon E5-2697 v4	EPYC 9554
Architecture	Broadwell	Zen4
SIMD capability	AVX2 (256bit)	AVX512 (512bit)
Base clock speed	2.3 GHz	3.1 GHz
L2 cache per socket	4.5 MB	64 MB
L3 cache per socket	45 MB	256 MB
Memory	4-ch DDR4-2400	12-ch DDR5-4800
Cores per socket	18	64
Socket per node	2	2
Peak GFLOPS per node	1152	7611
Compiler and flags	GCC 12.2.0, -O3	GCC 11.4.0, -O3
Parallel library	Open MPI 4.1.4	Open MPI 4.1.2
Profiler	likwid 5.2.0	likwid 5.4.1

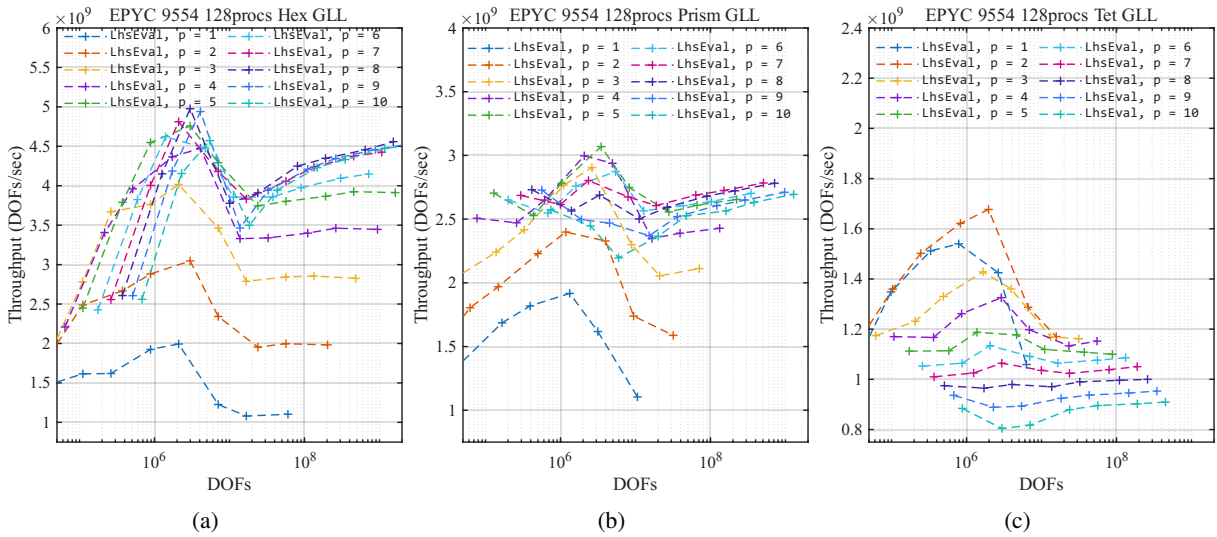


Figure 11: The throughput versus problem sizes (DOFs) and element orders, tested on EPYC 9554. (a) hexahedrons; (b) Prisms; (c) Tetrahedrons.

- We target arbitrary unstructured meshes filled with various shape types, so we miss many optimisations specialised for hexahedra-only meshes, making it difficult to achieve the same performance as reported in other work.
- deal.II includes structured affine meshes consisting of identical hexahedral elements with shared Jacobian and geometric data. This has significantly lower memory loading requirements and increase operation intensity.
- deal.II also uses Hermite polynomials for the element basis, which allows the evaluation of derivatives on traces from two layers of points. On the contrary, for the element bases we listed in Table 1, the whole element space is always needed to evaluate the derivative, which is theoretically more expensive.
- Dune uses a different vectorisation strategy: instead of evaluating 4 elements at a time, they evaluate 1 solution and 3 derivatives at the same time, by the same sum-factorisation kernel. To fill the 512-bit register, they also need to pack data on different points, so the data layout is more complicated.

## 5.2 Performance benchmarking

The performance benchmarks are performed on two different CPU computing nodes. The older machine has two Xeon E5-2697 v4 Broadwell CPUs with AVX2, mostly for comparison with the previous studies. The newer machine has two EPYC 9554 CPUs with AVX512. The detailed specifications of the hardware and software environment are summarised in Table 3.

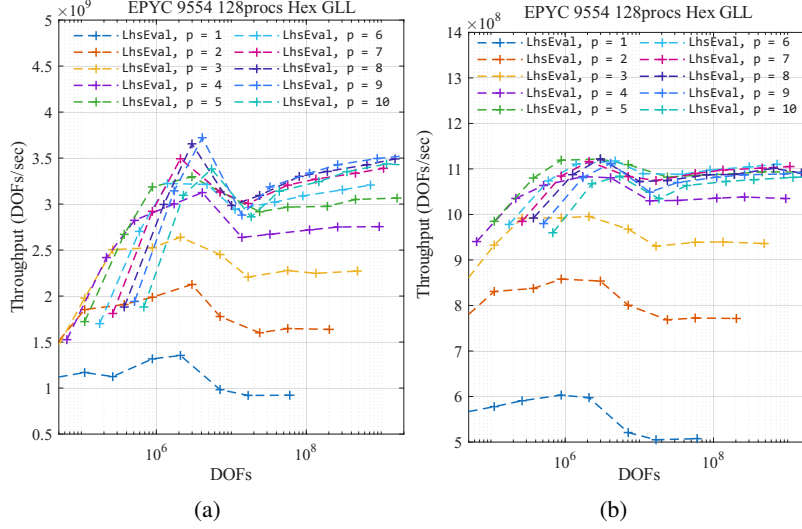


Figure 12: Throughput vs. problem sizes (DOFs) and element order, tested on EPYC 9554, for simulated non-conformal interfaces via (a) interpolation or (b) TraceIPProduct on element boundaries.

We focus on the maximum performance that can be achieved using all cores of a given node. Throughput is used to measure the performance, which is the number of degrees of freedom (DOF) processed per second by the target operator, calculated based on the elapsed time of the operator and the total DOFs it processes. Floating-point operations per second (FLOPS) can indicate how much potential we have exploited from the machine, which is obtained via the profiling tool suite `likwid`.

The throughput is affected by many factors: the spectral element shapes, basis order and quadrature order directly determine the computing complexity, whilst different problem sizes affect cache utilisation. Fig. 11 gives an overview of the throughput of LHS evaluation for varying DOFs, element orders and shapes. For brevity, we only test the modal basis functions with  $p + 2$  GLL (or  $p + 1$  GR) points along each coordinate. All the meshes we used for benchmarks are structured, such as  $64^3$  and  $48^3$ , but the code treats them as general unstructured meshes. No special techniques are applied during the pre-processing to improve performance. As the problem size increases, the throughput first increases to the peak at around  $10^6$  DOFs, where the cache performance is maximised; thereafter, the throughput experiences a short decline and soon recovers and levels off. Cache blocking techniques ensure that the memory access pattern is nearly independent of the data size, and so is the performance. For hexahedral and prismatic elements, increasing  $p$  from 1 to 5 significantly improves the performance, but for tetrahedral elements, increasing the order reduces the performance. The reason is twofold. When we fix the problem size and increase the order, the mesh will be sparser, but local element operations are denser, leading to better performance. However, increasing the order also increases the computing complexity, which should reduce the performance. For tetrahedral elements, the second reason dominates, and their operators cannot be optimised to the same level as hexahedral ones due to the variable loop counts.

A simple way to evaluate the performance in processing non-conforming interfaces is to force the use of TraceIPProduct or interpolation on all interfaces, even if the discretisation is conforming. Fig. 12 provides these results and can be directly compared with Fig. 11. We see that interpolation incurs around 30% performance loss with respect to the conformal case, but it is still significantly faster than TraceIPProduct. One factor is that the existing framework performs kernel fusing and cache blocking based on the element rather than the trace. Thus, some optimisation cannot be applied to TraceIPProduct in the same way as `ScatrInterp`. In this work, we primarily focus on the performance characteristics of interpolation approach.

Most previous studies choose a single mesh for each order for the performance benchmark, which produces more concise results, highlighting the difference between orders. The problem size is significantly bigger than the L3 caches, reflecting typical workloads. For the Xeon node, the tested problem sizes are around  $1 \times 10^7$  DOFs. The throughput results are shown in Fig. 13. The maximum throughput we achieved is about  $4 \times 10^8$  DOFs/s on the Broadwell CPU, lower than the *fusion* design given in [38], but still comparable to their *hybrid* design. The throughput of two sub-operators, `HelmholtzDGwithAverJump` and `HelmholtzIPDGTraceFlux`, gradually deviate from each other as the order increases. This is expected because the difference between element space and trace space grows larger for higher orders, and the volume flux also needs more operations to evaluate than the interface flux.

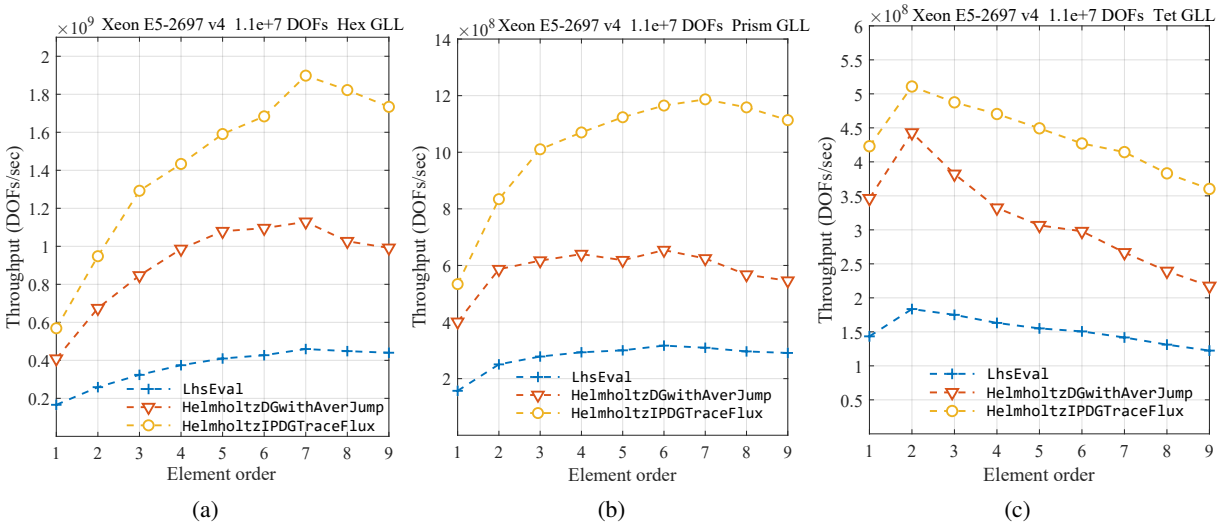


Figure 13: The throughput versus element order, tested on Xeon E5-2697 v4, with fixed-size ( $1.1 \times 10^7$  DOFs) hexahedral (a), prismatic (b) and tetrahedral (c) meshes.

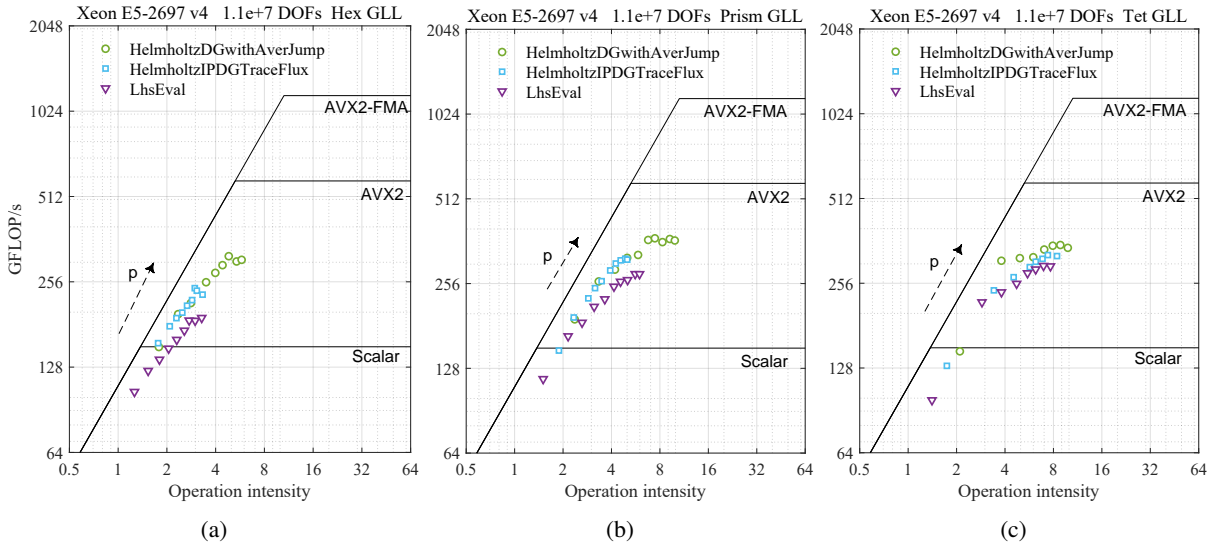


Figure 14: The roofline results obtained on Xeon E5-2697 v4. The order increases from 1 to 10 as shown by the arrow. (a) Hexahedrons; (b) Prisms; (c) Tetrahedrons.

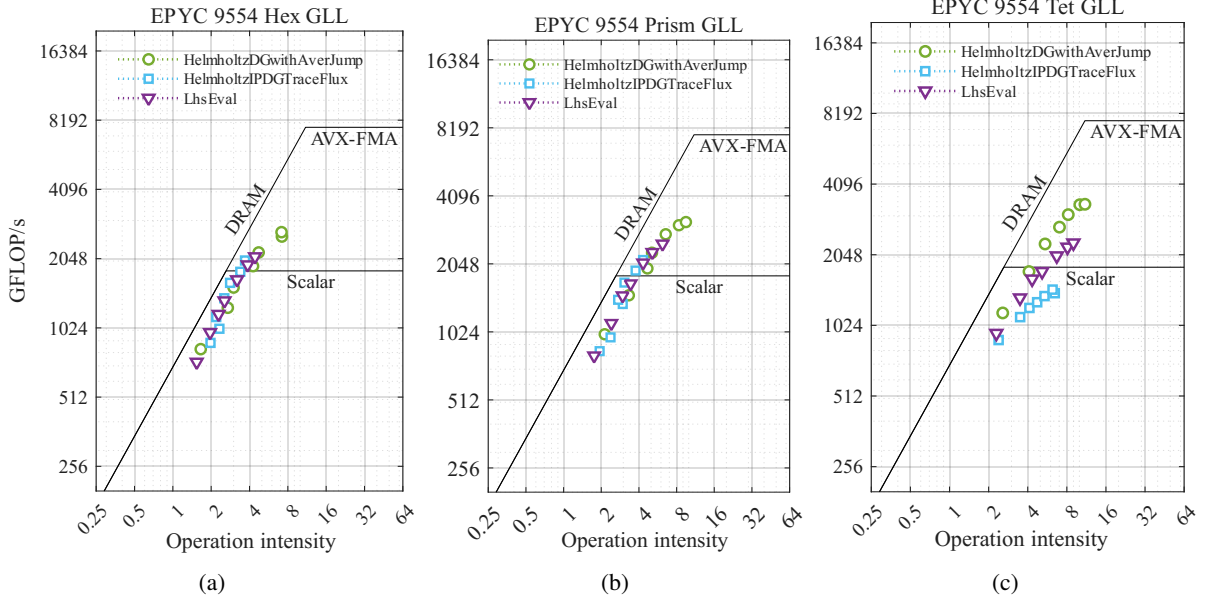


Figure 15: The roofline results obtained on EPYC 9554. The orders are 1,2,3,4,6,8,10. (a) Hexahedrons; (b) Prisms; (c) Tetrahedrons.

Finally, we present roofline results to show the utilisation of the hardware. Our previous studies, e.g. [26], demonstrated that the Helmholtz volume operations can reach AVX2 peak FLOPS on the same Xeon node. As a comparison, we present roofline results on the same machine for the `LhsEval` and two sub-operators in Fig. 15. The test case size is consistently set to  $1.1 \times 10^7$  DOFs for each order. For this Xeon node, we highlight 3 peak FLOPS rooflines obtained by `likwid-bench`. The highest corresponds to the theoretical peak of the CPU, which can only be achieved with perfect use of AVX2 and fused-multiply add operations (FMA); the second highest is the peak FLOPS achievable without FMA; and the lowest indicates the peak level without the use of any vectorisation. The two sub-operators fall between the second and the third line, roughly 20-30% of peak FLOPS, but still lower than the results reported by [39]. The roofline results obtained on the EPYC node are displayed in Fig. 14. The difference between FMA, AVX512, and AVX2 peak FLOPS is marginal on this node owing to the implementation of AVX512 on EPYC CPUs, resulting in only two distinct rooflines. The tested problem size exceeds  $1 \times 10^8$  DOFs to exhaust memory and cache bandwidth. Generally, as the order increases, both FLOPS and operational intensity rise, yet they remain evidently memory-bound. Tetrahedral elements achieve slightly higher FLOPS and also higher operation intensity than other shapes. The operation intensity is similar on the two machines, which is more related to the design itself. We will seek further optimisation in a later work, e.g., more aggressive kernel fusing and tuning the cache block size, in order to increase the operation intensity.

## 6 Conclusions

In this work, we have discussed the evaluation of the interface flux terms for DG methods, from formulation to implementation, aiming at a unified and low-cost DG framework for general spectral elements of different choices of shape, basis and quadrature. We have introduced an optimised matrix-free workflow for the DG solver. The key idea of the workflow is that all terms should be evaluated in the physical space, and only at the end do we transform physical space to coefficient space. Unlike collocated nodal elements, the transformation between coefficient space and physical space in a general spectral element is relatively expensive. So in this workflow, we reduce the number of transform operations to only two: a `BwdTrans` at the beginning, and an `IProduct` at the end.

The key operators that bridge the traces and elements have been discussed in detail. First, we identify two ways to get trace data from elements, `TracePhysEval` and `GathrInterp`. They are initially designed for Gauss and Gauss-Lobatto points, respectively, but can be generalised for all cases if necessary, and they are numerically equivalent. We then identify two ways to handle non-conforming interfaces, such as different polynomial orders between adjacent elements. For SIPG methods, this is critical since the system matrix can easily become non-symmetric if interface flux terms are inconsistent across the non-conforming interfaces, which finally causes conjugate gradient iterations to fail to converge. To resolve this issue, the first strategy is to unify the quadrature and flux evaluation on both sides,

by defining the shared trace space. The second strategy is to use sufficient quadrature points so that we can directly interpolate local element data to the adjacent side and evaluate the flux locally, known as point-to-point interpolation. The shared trace space approach is mathematically equivalent to the mortar element method, but we only copy data between physical spaces, instead of performing the  $L^2$  projection using the inverse mass matrix, making it much cheaper. In this work, we only focus on the polynomial non-conforming instead of geometric non-conforming in the discussion and numerical tests, although this extension is theoretically possible for both approaches.

Finally, an initial matrix-free implementation based on the optimised workflow is provided in detail. We exploit the performance on CPUs by improving cache data reuse and using explicit SIMD instructions. The interpolation approach via `ScatInterp` has been proven to be much more efficient than performing `TraceIPProduct` on shared traces, regardless of whether they are conforming or not. This is an important reason why we still emphasise the implementation of the interpolation approach in the current work, although it has numerical defects. We aim at unstructured meshes with hybrid element types, so it is naturally more difficult to optimise. Although our design does not achieve the highest performance in comparison to other studies, we enabled an efficient design for various element types and also non-conforming meshes. We have provided performance benchmark results for various problem sizes, element orders, and shape types, which can be a good reference for those interested in performance topics. Aside from optimising the matrix-free implementation, future work will also focus on large-scale parallel computing, with a particular focus on reducing communication overheads and effective preconditioning strategies.

## A Relationship between flux terms and symmetry of system matrix

Assume there are two overlapping elemental boundaries,  $\Gamma_r$  and  $\Gamma_l$ , from two adjacent element  $\Omega_r$  and  $\Omega_l$ . We use  $r$  and  $l$  to distinguish the right and left side objects. For instance, the bases of two elements are  $\phi_i^r, \phi_i^l$  and coefficients are  $\hat{u}_i^r, \hat{u}_i^l$ . The unit normals always point outwards on the elemental boundary, so  $\mathbf{n}^l = -\mathbf{n}^r$ . With these notations, the three flux terms in Eq. (4) become

$$\text{Symmetry flux added to the left element : } -(\nabla\phi_i^l \cdot \mathbf{n}^l, \phi_j^l)_{\Gamma_l} \frac{1}{2} \hat{u}_j^l + (\nabla\phi_i^l \cdot \mathbf{n}^l, \phi_j^r)_{\Gamma_l} \frac{1}{2} \hat{u}_j^r$$

$$\text{Trace flux added to the left element : } -(\phi_i^l, \mathbf{n}^l \cdot \nabla\phi_j^l)_{\Gamma_l} \frac{1}{2} \hat{u}_j^l - (\phi_i^l, \mathbf{n}^l \cdot \nabla\phi_j^r)_{\Gamma_l} \frac{1}{2} \hat{u}_j^r$$

$$\text{Penalty flux added to the left element : } \tau(\phi_i^l, \phi_j^l)_{\Gamma_l} \hat{u}_j^l - \tau(\phi_i^l, \phi_j^r)_{\Gamma_l} \hat{u}_j^r$$

Flux added to the right side can be written down similarly. Here, we deliberately perform the inner product in the local element boundaries to show how it affects symmetry of the system. Now we collect contributions from the left and right sides:

$$\begin{aligned} \text{Left to left : } & \left[ \begin{array}{ccc} \mathbf{M}_A & \mathbf{M}'_A & \mathbf{M}_E \\ -(\phi_i^l, \mathbf{n}^l \cdot \nabla\phi_j^l)_{\Gamma_l} & -(\nabla\phi_i^l \cdot \mathbf{n}^l, \phi_j^l)_{\Gamma_l} & +2\tau(\phi_i^l, \phi_j^l)_{\Gamma_l} \end{array} \right] \frac{1}{2} \hat{u}_j^l \\ \text{Right to right : } & \left[ \begin{array}{ccc} \mathbf{M}_B & \mathbf{M}'_B & \mathbf{M}_F \\ -(\phi_i^r, \mathbf{n}^r \cdot \nabla\phi_j^r)_{\Gamma_r} & -(\nabla\phi_i^r \cdot \mathbf{n}^r, \phi_j^r)_{\Gamma_r} & +2\tau(\phi_i^r, \phi_j^r)_{\Gamma_r} \end{array} \right] \frac{1}{2} \hat{u}_j^r \\ \text{Right to left : } & \left[ \begin{array}{ccc} \mathbf{M}_C & \mathbf{M}'_D & \mathbf{M}_G \\ -(\phi_i^l, \mathbf{n}^l \cdot \nabla\phi_j^r)_{\Gamma_l} & +(\nabla\phi_i^l \cdot \mathbf{n}^l, \phi_j^r)_{\Gamma_l} & -2\tau(\phi_i^l, \phi_j^r)_{\Gamma_l} \end{array} \right] \frac{1}{2} \hat{u}_j^r \\ \text{Left to right : } & \left[ \begin{array}{ccc} \mathbf{M}_D & \mathbf{M}'_C & \mathbf{M}'_G \\ -(\phi_i^r, \mathbf{n}^r \cdot \nabla\phi_j^l)_{\Gamma_r} & +(\nabla\phi_i^r \cdot \mathbf{n}^r, \phi_j^l)_{\Gamma_r} & -2\tau(\phi_i^r, \phi_j^l)_{\Gamma_r} \end{array} \right] \frac{1}{2} \hat{u}_j^l \end{aligned}$$

The locations of these elemental matrices in the system matrix are:

$$\begin{bmatrix} -\mathbf{M}_A - \mathbf{M}'_A + \mathbf{M}_E & \cdots & -\mathbf{M}_C + \mathbf{M}'_D - \mathbf{M}_G \\ \cdots & \ddots & \cdots \\ \mathbf{M}'_C - \mathbf{M}_D - \mathbf{M}'_G & \cdots & -\mathbf{M}_B - \mathbf{M}'_B + \mathbf{M}_F \end{bmatrix}$$

Matrices A, B, E, and F are added to the diagonal entries of the blocked system matrix, while C, D, and G are added to the off-diagonal entries. To get a symmetric system, we must ensure

$$\mathbf{M}'_A = \mathbf{M}_A^T, \quad \mathbf{M}'_B = \mathbf{M}_B^T, \quad \mathbf{M}'_E = \mathbf{M}_E^T, \quad \mathbf{M}'_F = \mathbf{M}_F^T$$

and

$$\mathbf{M}'_C = -\mathbf{M}_C^T, \quad \mathbf{M}'_D = -\mathbf{M}_D^T, \quad \mathbf{M}'_G = \mathbf{M}_G^T$$

The first relation is always satisfied. As for the second one, we must ensure that quadrature on the overlapped boundaries  $\Gamma_l \Gamma_r$  are either the same or have sufficient accuracy.

## References

- [1] Z.J. Wang, Krzysztof Fidkowski, Rémi Abgrall, Francesco Bassi, Doru Caraeni, Andrew Cary, Herman Deconinck, Ralf Hartmann, Koen Hillewaert, H.T. Huynh, Norbert Kroll, Georg May, Per-Olof Persson, Bram van Leer, and Miguel Visbal. High-order CFD methods: current status and perspective: HIGH-ORDER CFD METHODS. *Int. J. Numer. Meth. Fluids*, 72(8):811–845, July 2013.
- [2] J.-E. W. Lombard, D. Moxey, S. J. Sherwin, J. F. A. Hoessler, S. Dhandapani, and M. J. Taylor. Implicit large-eddy simulation of a wingtip vortex. *AIAA J.*, 54(2):506–518, 2016.
- [3] F. F. Buscariolo, J. Hoessler, D. Moxey, A. Jassim, K. Gouder, J. Basler, Y. Murai, G. R. S. Assi, and S. J. Sherwin. Spectral/*hp* element simulation of flow past a formula one front wing: validation against experiments. *J. Wind. Eng. Ind. Aerod.*, 221:104832, 2022.
- [4] J. Slaughter, D. Moxey, and S. J. Sherwin. Large eddy simulation of an inverted multi-element wing in ground effect. *Flow Turbul. Combust.*, (110):917–944, 2023.
- [5] G. Mengaldo, D. Moxey, M. Turner, R. C. Moura, A. Jassim, M. Taylor, J. Peiró, and S. J. Sherwin. Industry-relevant implicit large-eddy simulation of a high-performance road car via spectral/*hp* element methods. *SIAM Review*, (4):723–755, 2021.
- [6] D. Moxey, M. D. Green, S. J. Sherwin, and J. Peiró. An isoparametric approach to high-order curvilinear boundary-layer meshing. *Comp. Meth. Appl. Mech. Eng.*, 283:636–650, 2015.
- [7] Martin Kronbichler and Wolfgang A. Wall. A performance comparison of continuous and discontinuous Galerkin methods with fast multigrid solvers. *SIAM J. Sci. Comp.*, 40(5):A3423–A3448, 2018.
- [8] Peter Bastian, Felix Heimann, and Sven Marnach. Generic implementation of finite element methods in the distributed and unified numerics environment (DUNE). *Kybernetika*, 46(2):294–315, 2010.
- [9] Freddie D. Witherden, Antony M. Farrington, and Peter E. Vincent. PyFR: An open source framework for solving advection–diffusion type problems on streaming architectures using the flux reconstruction approach. *Comp. Phys. Comm.*, 185(11):3028–3040, 2014.
- [10] Freddie D Witherden, Peter E Vincent, Will Trojak, Yoshiaki Abe, Amir Akbarzadeh, Semih Akkurt, Mohammad Alhawary, Lidia Caros, Tarik Dzanic, Giorgio Giangaspero, et al. Pyfr v2. 0.3: Towards industrial adoption of scale-resolving simulations. *Comp. Phys. Comm.*, page 109567, 2025.
- [11] Julian Andrej, Nabil Atallah, Jan-Phillip Bäcker, Jean-Sylvain Camier, Dylan Copeland, Veselin Dobrev, Johann Dudouit, Tobias Duswald, Brendan Keith, Dohyun Kim, et al. High-performance finite elements with mfem. *The International Journal of High Performance Computing Applications*, 38(5):447–467, 2024.
- [12] Tzanio Kolev, Paul Fischer, Misun Min, Jack Dongarra, Jed Brown, Veselin Dobrev, Tim Warburton, Stanimire Tomov, Mark S Shephard, Ahmad Abdelfattah, et al. Efficient exascale discretizations: High-order finite element methods. *The International Journal of High Performance Computing Applications*, 35(6):527–552, 2021.
- [13] Francesco Bassi and Stefano Rebay. A high-order accurate discontinuous finite element method for the numerical solution of the compressible navier–stokes equations. *J. Comp. Phys.*, 131(2):267–279, 1997.
- [14] Douglas N. Arnold, Franco Brezzi, Bernardo Cockburn, and L. Donatella Marini. Unified Analysis of Discontinuous Galerkin Methods for Elliptic Problems. *SIAM J. Numer. Anal.*, 39(5):1749–1779, January 2002.
- [15] Bernardo Cockburn, George E. Karniadakis, and Chi-Wang Shu, editors. *Discontinuous Galerkin methods: theory, computation and applications*, volume 11 of *Lecture Notes in Computational Science and Engineering*. Springer Berlin, Heidelberg, 2012.
- [16] Steven A Orszag. Spectral methods for problems in complex geometries. *Journal of Computational Physics*, 37(1):70–92, August 1980.

- [17] Niklas Fehn, Wolfgang A. Wall, and Martin Kronbichler. On the stability of projection methods for the incompressible NavierStokes equations based on high-order discontinuous Galerkin discretizations. *Journal of Computational Physics*, 351:392–421, December 2017.
- [18] Niklas Fehn, Wolfgang A. Wall, and Martin Kronbichler. Robust and efficient discontinuous Galerkin methods for under-resolved turbulent incompressible flows. *Journal of Computational Physics*, 372:667–693, November 2018.
- [19] Peter Bastian, Eike Hermann Müller, Steffen Müthing, and Marian Piatkowski. Matrix-free multigrid block-preconditioners for higher order discontinuous Galerkin discretisations. *Journal of Computational Physics*, 394:417–439, October 2019.
- [20] Niklas Fehn, Peter Munch, Wolfgang A. Wall, and Martin Kronbichler. Hybrid multigrid methods for high-order discontinuous Galerkin discretizations. *Journal of Computational Physics*, 415:109538, August 2020.
- [21] E. Ferrer, G. Rubio, G. Ntoukas, W. Laskowski, O. A. Mariño, S. Colombo, A. Mateo-Gabín, H. Marbona, F. Manrique de Lara, D. Huergo, J. Manzanero, A. M. Rueda-Ramírez, D. A. Kopriva, and E. Valero. Horses3D: A high-order discontinuous Galerkin solver for flow simulations and multi-physics applications. *Computer Physics Communications*, 287:108700, June 2023.
- [22] Niclas Jansson, Martin Karp, Artur Podobas, Stefano Markidis, and Philipp Schlatter. Neko: A modern, portable, and scalable framework for high-fidelity computational fluid dynamics. *Computers & Fluids*, 275:106243, May 2024.
- [23] Nico Pietroni, Marcel Campen, Alla Sheffer, Gianmarco Cherchi, David Bommers, Xifeng Gao, Riccardo Scateni, Franck Ledoux, Jean Remacle, and Marco Livesu. Hex-mesh generation and processing: a survey. *ACM Transactions on Graphics*, 42(2):1–44, 2022.
- [24] George Karniadakis and Spencer J. Sherwin. *Spectral/hp element methods for CFD*. Numerical mathematics and scientific computation. Oxford University Press, New York, 1999.
- [25] T.C. Warburton, I. Lomtev, Y. Du, S.J. Sherwin, and G.E. Karniadakis. Galerkin and discontinuous Galerkin spectral/hp methods. *Computer Methods in Applied Mechanics and Engineering*, 175(3-4):343–359, July 1999.
- [26] David Moxey, Roman Amici, and Mike Kirby. Efficient Matrix-Free High-Order Finite Element Evaluation for Simplicial Elements. *SIAM J. Sci. Comput.*, 42(3):C97–C123, January 2020.
- [27] David A. Kopriva. A Staggered-Grid Multidomain Spectral Method for the Compressible NavierStokes Equations. *Journal of Computational Physics*, 143(1):125–158, June 1998.
- [28] Yvon Maday, Cathy Mavriplis, and Anthony T. Patera. Nonconforming mortar element methods - application to spectral discretizations. In *Domain Decomposition Methods*, pages 392–418, January 1989.
- [29] Catherine Mavriplis. A posteriori error estimators for adaptive spectral element techniques. In Pieter Wesseling, editor, *Proceedings of the Eighth GAMM-Conference on Numerical Methods in Fluid Mechanics*, pages 333–342, Wiesbaden, 1990. Vieweg+Teubner Verlag.
- [30] David A. Kopriva, Stephen L. Woodruff, and M. Y. Hussaini. Computation of electromagnetic scattering with a nonconforming discontinuous spectral element method. *Numerical Meth Engineering*, 53(1):105–122, January 2002.
- [31] Edward Laughton, Gavin Tabor, and David Moxey. A comparison of interpolation techniques for non-conformal high-order discontinuous Galerkin methods. *Computer Methods in Applied Mechanics and Engineering*, 381:113820, August 2021.
- [32] Johannes Heinz, Peter Munch, and Manfred Kaltenbacher. High-order non-conforming discontinuous Galerkin methods for the acoustic conservation equations. *International Journal for Numerical Methods in Engineering*, 124(9):2034–2049, 2023.
- [33] Jakob Dürrwächter, Marius Kurz, Patrick Kopper, Daniel Kempf, Claus-Dieter Munz, and Andrea Beck. An efficient sliding mesh interface method for high-order discontinuous Galerkin schemes. *Computers & Fluids*, 217:104825, March 2021.
- [34] E. Laughton, V. Zala, A. Narayan, R. M. Kirby, and D. Moxey. Fast barycentric-based evaluation over spectral/hp elements. *J. Sci. Comp.*, 90:78, 2022.
- [35] Michael G. Duffy. Quadrature over a pyramid or cube of integrands with a singularity at a vertex. *SIAM J. Sci. Comp.*, 19(6):1260–1262, 1982.
- [36] Paul Fischer, Misun Min, Thilina Rathnayake, Som Dutta, Tzanio Kolev, Veselin Dobrev, Jean-Sylvain Camier, Martin Kronbichler, Tim Warburton, Kasia wirydownicz, and Jed Brown. Scalability of high-performance PDE

- solvers. *The International Journal of High Performance Computing Applications*, 34(5):562–586, September 2020.
- [37] Martin Kronbichler and Katharina Kormann. Fast Matrix-Free Evaluation of Discontinuous Galerkin Finite Element Operators. *ACM Trans. Math. Softw.*, 45(3):1–40, September 2019.
- [38] Dominic Kempf, René HeSS, Steffen Müthing, and Peter Bastian. Automatic Code Generation for High-performance Discontinuous Galerkin Methods on Modern Architectures. *ACM Trans. Math. Softw.*, 47(1):6:1–6:31, December 2020.
- [39] Steffen Müthing, Marian Piatkowski, and Peter Bastian. High-performance Implementation of Matrix-free High-order Discontinuous Galerkin Methods, November 2017. arXiv:1711.10885 [math].